Proof of Concept for a Smart Composite Orbital Debris Detector

[1]Mario Emanuele DE SIMONE, [1]Christos ANDREADES, [1]Amin Mohamad HILMI, [1]Michele MEO, [2]Francesco CIAMPA[*]

[1]Department of Mechanical Engineering, University of Bath, Bath BA2 7AY, UK

[2]Department of Mechanical Engineering Sciences, University of Surrey, Guildford GU2 7XH, UK

[*]corresponding author: f.ciampa@surrey.ac.uk

ABSTRACT

Space debris particles with dimensions smaller than tens of millimetres are not trackable with existing monitoring systems and have sufficient energy to harm orbiting Earth satellites during impact events. This paper presents a proof-of-concept for an in-situ smart carbon fibre reinforced plastic (CFRP) composite orbital debris detector that is capable of localising space debris impacts on Earth satellites and measuring the direction and velocity of debris particles. This spacecraft detection system can be used to warn satellites about the impact occurrence and to enhance current Space Surveillance Networks by providing a catalogue of debris objects. The proposed orbital debris detector consists of two thin parallel CFRP composite plates, each instrumented with three piezoelectric transducers embedded into the laminate. The localisation method is based on the measurement of acoustic emissions generated by debris impacts on the CFRP plates, which are processed with the time reversal algorithm. The calculation of the direction of debris particles and their speed are accomplished by determining the arrival time of acquired signals and the speed of waves propagating within each CFRP plate. Experimental results showed accurate estimation of the impact location, direction and velocity, thus demonstrating the potential use of the proposed orbital debris detector in future Earth satellite systems.

Keywords: Space debris, impact localisation, time reversal, composite materials, embedded sensors.

1 INTRODUCTION

Space debris accounts for about 95% of human-made orbiting objects in the outer space [1] and includes non-functional entities such as fragments and elements orbiting around the Earth or re-entering the Earth's atmosphere [2]. In Low Earth Orbit (LEO), space debris speeds are typically around 7 - 10 km/s [3] and impacts at these velocities are commonly referred to as "hypervelocity impacts" (HVIs). In HVIs, the impact speed is such that the strength of materials upon impact is sufficiently small compared to their inertial forces [4], [5]. As a result, high impact energies are achieved even with small particles having dimensions ranging between 10 μm and few mm, which are sufficient to harm the orbiting spacecraft. Large objects (> 1 - 10 cm) would, instead, destroy or severely damage the satellite [6]. Debris particles greater than few tens of mm are generally detectable with current optical systems (e.g. telescopes [7], [8]), so that collision avoidance measures can be taken. These include mitigation and remediation methods, and active debris removal technologies. Mitigation methods involve the use of space debris models for mission risk analysis and debris population such as the ESA's Meteoroid and Space Debris Terrestrial Environment Reference (MASTER) and NASA's Orbital Debris Engineering Model (ORDEM) series [9]-[11], as well as space debris tracking and monitoring systems such as the NASA Meter-Class Autonomous Telescope [8]. Remediation methods are, for example, spacecraft shields used to protect the spacecraft against impacts from untracked debris [12]. Whipple shield and its variations such as Multi-Shock and Stuffed Whipple shields [13] are the most widely used protection systems on modern spacecrafts. Active debris removal is, lately, the most effective yet the most challenging measure against space debris. Some examples of space debris removal technologies include satellite drag sails [14], hybrid propulsion for re-entry after service [1] and debris capture systems using the space net [15]. However, these technologies still need years or even decades for full implementations to take place.

Nevertheless, all above mentioned technologies do not currently allow protection from small debris particles, which are not trackable nor visible with existing observation systems. Hence, mitigation

strategies including the development of *in-situ* passive space debris detectors carried on satellites are required to minimise the failure risk of future unmanned spacecrafts and manned operational space stations (e.g. the International Space Station) [6]. In particular, *in-situ* passive detectors can provide in-service monitoring of spacecraft components and are able to characterise space debris population by measuring the trajectory (direction), the time of impact and velocity of particles. This information is of fundamental importance to (*i*) understand the orbital dynamics of space debris, (*ii*) allow rapid warning to orbiting satellites of the impact occurrence, (*iii*) enhance current Space Surveillance Networks by providing an accurate catalogue of debris objects of various dimensions and (*iv*) validate existing numerical models for the orbital prediction of space debris with experimental orbital data [9].

For this scope, a number of passive debris detection systems have been proposed and validated in literature. Burchell et al. [16], [17] investigated a debris sensing technology using a resistive grid sensitive to hypervelocity impacts. In this concept, the particle penetration of a thin substrate with a resistive grid enabled changes to the overall grid resistance. These changes were proportional to the perforation area that, in turn, was related to the debris particle's size. This detection system was validated with particles of 0.15 mm diameter and above. Bauer et al. [18] recently developed the Solar Panel based Space Debris Impact Detector (SOLID) that uses an autonomous electronic box implemented into the spacecraft and solar panel structures to monitor impact damage. Forli [19] and Schäfer and Janovsky [20] used acoustic emission based impact sensor networks to detect HVIs. Graziani et al. [21] developed an impact debris detector that was installed on the UNISAT microsatellite and used piezoelectric (PZT) patches for on-board monitoring of the micro-particle environment.

Regarding to the elastic wave propagation in solids after HVIs, Liu et al. [4], [5] demonstrated that HVI-induced shock waves generated at the impact spot convert rapidly into standard elastic waves. Standards waves can be, therefore, measured by traditional signal detection systems to provide information about the impact location. Kobayashi et al. [22] recently developed the Circum-Martian

Dust Monitor (CMDM) system consisting of a thin film and PZT sensors, which will be used in the JAXA's Martian Moons Exploration (MMX) project. Corsaro et al. [23] conducted an experiment to characterise space dust using acoustic emissions. Their system was inspired by the multi-layer spacecraft shielding technology and consisted of two pairs of four Polyvinylidene Fluoride (PVDF) sensors placed on two parallel Mylar thin films to provide impact location. In Corsaro et al.'s work, triangulation techniques based on accurate time-of-flight measurements were used to identify the impact location and determine the impact direction and velocity of debris objects. However, such a debris detection system was affected by the uncertainty of the time of arrival estimation, which may cause large errors on the impact location. Moreover, the use of Mylar films required PVDF sensors to be exposed to the outer space.

This paper builds on Corsaro et al.'s work [23] and aims at developing an *in-situ* and lightweight "Smart Composite Orbital Debris Detector (SCODD)" based on acoustic emission measurements, which is capable of localising space debris impacts and measuring the direction and velocity of debris particles. The proposed SCODD system consists of two sacrificial thin parallel carbon fibre reinforced plastic (CFRP) composite plates, which are instrumented with three embedded PZTs located at the middle layer of each plate. The two CFRP samples were manufactured thin enough so that they can be easily penetrated by the debris particles without significantly slowing their orbital speed. As a result, the impact energy attenuation during penetration can be neglected even with small debris objects. The technology for embedding PZT transducers into CFRP laminates was recently developed by the authors and reported in Andreades et al.'s paper [24]. The implementation of embedded acoustic transducers, as in the proposed SCOOD system, represents more practical approaches for space applications where harsh space environmental conditions such as extreme temperatures and high levels of radiation and humidity may easily degrade surface mounted piezo-films and exposed transducers. Moreover, for the accurate impact localisation in both plates, time reversal (TR) method was used (see, for instance, [25]-[29]). Debris particle directions and velocity were then calculated by determining the arrival times (TOAs) of acquired waveforms and the speed

of waves propagating in the CFRP specimens. TOAs were obtained by using the Akaike Information Criterion method, which provides the onset time of a recorded signal with microseconds of precision [30]. The outline of this research work is as follows: in Section 2, the SCODD system is presented. The particle direction calculation is shown in Section 3, whose main parts are the time reversal method for the impact localisation in Section 3.1, and the angular parameters identifying the particle direction of arrival in Section 3.2. The particle speed is the topic of Section 4. Section 5 shows the set-up used to perform experimental tests, whilst in Section 6 all the experimental impact results are illustrated. The conclusions of this paper are presented in Section 7.

2 SMART COMPOSITE ORBITAL DEBRIS DETECTOR

The objectives of the SCODD system are the impact location and the estimation of both direction and speed of debris objects impacting the detector. The proposed SCODD system is shown in Figure 1, in which S_i ($i = 1, 2, 3$) are the three piezoelectric transducers embedded in each CFRP laminate. In this concept, the space debris particle hit the thin CFRP top plate at the time t^* and continues along its trajectory towards the bottom one. The particle impacts the bottom sample at the time $t^* + \frac{s_p}{V_p}$, where V_p is the particle's velocity and s_p is the distance covered by the particle between the two impact points on the two plates. For clarity reasons, a two-dimensional illustration of the proposed SCODD system is represented in Figure 2. An impact perpendicular to both membranes is considered and only one couple of transducers, S_1, embedded at the same location on both plates is represented.

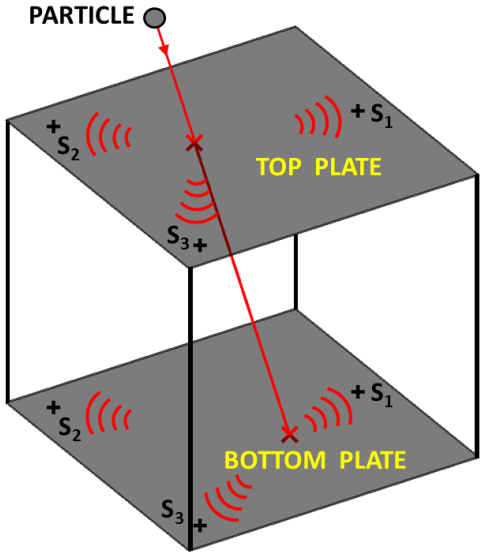

Figure 1. 3D sketch of the proposed SCODD system.

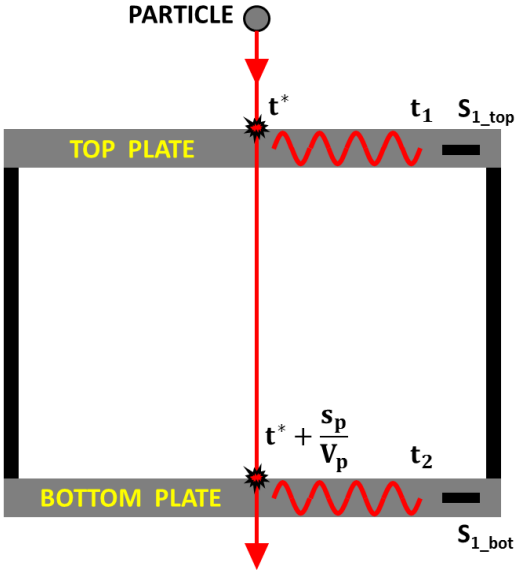

Figure 2. Illustration of the impacting debris particle perpendicular to the plane of both CFRP plates with embedded PZT transducers.

Acoustic waves generated by the impact on the top plate propagate along the membrane and are detected by the receiver transducer S_{1_top} at time t_1, whose mathematical expression is:

$$t_1 = t^* + \frac{r_1}{V_{w\_top}}, \tag{1}$$

where r_1 is the distance between the impact location and the position of the transducer S_{1_top} on the top plate. The velocity V_{w_top} is the propagation speed of the acoustic waves in the top plate and is calculated by using an initial calibration process (see Section 4.2 for details). After the particle

penetrates the bottom plate, elastic waves propagate into the sample and are acquired by the receiver sensor S_{1_bot} at time t_2, whose mathematical expression is:

$$t_2 = t^* + \frac{s_p}{V_p} + \frac{r_2}{V_{w\_bot}}. \quad (2)$$

Similarly to r_1, r_2 represents the distance between the impact location and the position of the transducer S_{1_bot} on the bottom plate. The particle velocity can be calculated by using the time difference Δt measured by the two embedded transducers:

$$\Delta t = t_2 - t_1 = \frac{s_p}{V_p} + \frac{r_2}{V_{w\_bot}} - \frac{r_1}{V_{w\_top}}. \quad (3)$$

The final expression for the speed of the debris particle is:

$$V_p = \frac{s_p}{\Delta t + \frac{r_1}{V_{w\_top}} - \frac{r_2}{V_{w\_bot}}}. \quad (4)$$

Since both CFRP plates are the same, we can assume $V_{w\_top} = V_{w\_bot}$. In the simple case of an impact perpendicular to both plates, the distance $r_1 \equiv r_2$ and

$$V_p = \frac{s_p}{\Delta t}. \quad (5)$$

It should be also noted that Eq. (4) considers only a couple of embedded transducers at the same locations on the two plates. In this work, a number of $N = 3$ embedded transducers was considered for the processing of time reversal, so N velocities were calculated. Following a calibration process of CFRP plates, the particle velocity was obtained as the mean of the N estimated velocities.

3 ESTIMATION OF SPACE DEBRIS LOCATION AND DIRECTION

In this Section, the algorithm for the estimation of the impact location and debris particle direction is presented. The particle trajectory (direction) is identified by two angular parameters, the "elevation", α, and the "azimuth", γ, which are measured in a horizontal coordinate system relative to the bottom plate.

3.1 IMPACT LOCALISATION ALGORITHM – TIME REVERSAL

A number of impact localisation algorithms were developed for both isotropic and anisotropic media [30]-[35]. In this work, the time reversal method is used to achieve high accuracy on the impact localisation for the SCODD system. TR is based on the hypothesis of time invariance and spatial reciprocity of the elastodynamic wave equation and on the Huygens' Principle, through which it is possible to reconstruct the wave function in a generic volume by the knowledge of its sources located on a two-dimensional surface. A detailed theoretical explanation of the TR method is presented in [25]-[29]. TR is typically divided into the "forward" and "backward" propagation steps. In the "forward" one, calibration impacts were applied in M excitation points, also called "calibration points", which were arbitrarily chosen on the plane of the plate (focusing plane) identifying the monitoring zone. A number of N receiving sensors were used, so that a set of $N \times M$ signals was acquired and stored in the computer memory. These waveforms represent the impulsive response of the single CFRP plate subject to impact loading. The "backward" propagation step consisted of correlating the waveform emitted by a point of unknown position $\mathbf{r}_{m0}$ with all the impulse responses stored in the "forward" step. It can be demonstrated that the impact location is calculated as the maximum of the following time reversal operator (i.e. when $\mathbf{r}_m = \mathbf{r}_{m0}$):

$$R_{TR} = G(\mathbf{r}_m, t;\ \mathbf{r}) \otimes G(\mathbf{r}, -t;\ \mathbf{r}_{m0}) = \int_0^t G(\mathbf{r}_m, t;\ \mathbf{r})\, G(\mathbf{r}, t+\tau;\ \mathbf{r}_{m0})\, d\tau\,, \tag{6}$$

which represents a cross correlation operation. The symbol $\otimes$ represents a convolution over time and $G(\cdot)$ denotes the Green space-time function. It should be noted that for the experimental campaign, given the existing facilities available, HVIs could not be performed during both "forward" and "backward" steps and low-velocity impacts were, instead, examined. However, the lower impact speed would not compromise the validity of the proof-of-concept for the proposed SCODD system. Indeed, in accordance with both numerical and experimental evidence reported by Liu et al. [4], [5] and Burchell et al. [16], [17], elastic modes recorded during low-velocity impacts resemble those generated after shock waves during HVIs. In particular, after HVI occurrence, pressure-induced shock

waves are immediately converted into standard elastic modes due to wave attenuation and diffraction distance [5]. Moreover, whilst shock waves require high speed data acquisition systems (~100 million samples per second), traditional bulk and guided waves involve lower signal acquisition rates [16], [17] and [20]. Hence, standard elastic modes can be used to retrieve the information of the impact location. For the TR process, signals at different elastic energies caused by low-velocity impacts were measured in the "forward" propagation step and a normalisation of the energy of acquired signals was performed. Such a normalisation allowed TR to be independent from the amplitude and, thus, from the elastic energy of recorded waveforms. Such a normalisation process is expressed as follows:

$$|R_{TR}| \leq \|G(\mathbf{r}_m, t;\ \mathbf{r})\|\ \|G(\mathbf{r}, t+\tau;\ \mathbf{r}_{m0})\| = \sqrt{E_{G\mathbf{r}_m}\ E_{G\mathbf{r}_{m0}}}\,, \tag{7}$$

where E_G is the waveform's elastic energy. As a measure of similarity of two signals, the time reversal correlation coefficient, c_{TR}, was used, which is defined as:

$$c_{TR} = \max\left(\frac{|R_{TR}|}{\sqrt{E_{G\mathbf{r}_m}\ E_{G\mathbf{r}_{m0}}}}\right). \tag{8}$$

Eq. (8) satisfies the inequality $0 \leq c_{TR} \leq 1$. The c_{TR} coefficient is close to one when the signals are similar (i.e. at the true impact location), whilst it is close to zero elsewhere. In order to compensate the incoherent measurement noise due to electronics, an average from the contribution of the N receiving sensors was here used and a single mean correlation coefficient was related to each grid node. According to Figure 3, each cell of the grid on the monitoring zone is identified by four nodes and it was possible to perform a further mean among the correlation coefficients associated to each node in order to calculate a global correlation coefficient of the cell, indicated as c_{TR_GLOBAL}.

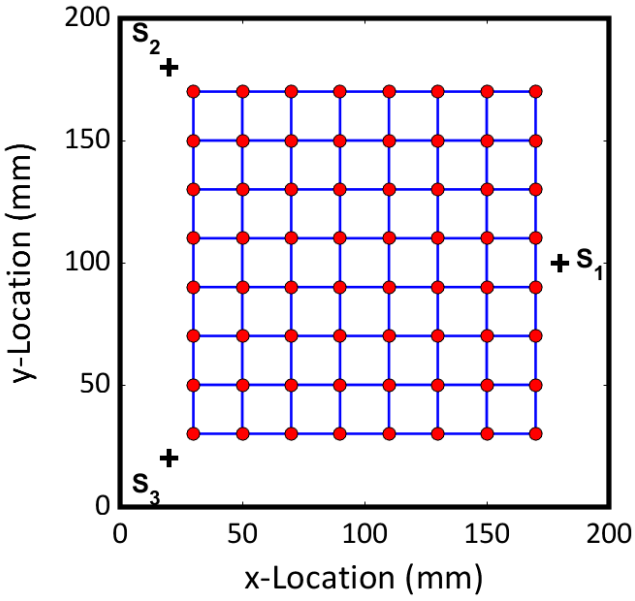

Figure 3. Initial surface grid. Calibration points are depicted as red spots.

Similarly to [36] and [37], the impact coordinates were finally estimated by the following centre-of-gravity method:

$$x_I = \frac{\sum_{i=1}^{4} x_i \, c_{TR_i}}{\sum_{i=1}^{4} c_{TR_i}}, \qquad y_I = \frac{\sum_{i=1}^{4} y_i \, c_{TR_i}}{\sum_{i=1}^{4} c_{TR_i}}, \tag{9}$$

where x_i and y_i are the coordinates of the i^{th} node of the impact cell, c_{TR_i} is the averaged correlation coefficient related to the i^{th} node, x_I and y_I are the estimated locations of the current impact event.

3.2 ESTIMATION OF THE PARTICLE DIRECTION PARAMETERS

Once obtained the coordinates of the impact locations on both plates, it is possible to evaluate the distance covered by the particle between the two impacts and its direction. A three-dimensional spherical coordinate system was used, in which a generic position vector, $\mathbf{s_p}$, joining two points in space is identified by the following three parameters:

- the Euclidean distance, $\mathbf{s_p}$, between the two points, which is the modulus of the position vector $\mathbf{s_p}$;
- the azimuth angle, γ, of the orthogonal projection of $\mathbf{s_p}$ on a reference plane passing through its origin and that is orthogonal to the zenith direction measured from a fixed reference

direction on that plane;

- the elevation angle, α, measured from the reference plane towards the direction of $\mathbf{s_p}$ and that is restricted to the interval $[0^\circ \ 90^\circ]$.

Figure 4 illustrates the described coordinate system related to SCODD. The origin of the Cartesian coordinate system is chosen as one of the corners of the bottom plate, which is considered as the reference *xy*-plane (the horizon). The *z*-axis is chosen to form the right-handed coordinate system, positive towards the corner of the top plate (i.e. the zenith). In the following figures the transducer numbers were not depicted for clarity.

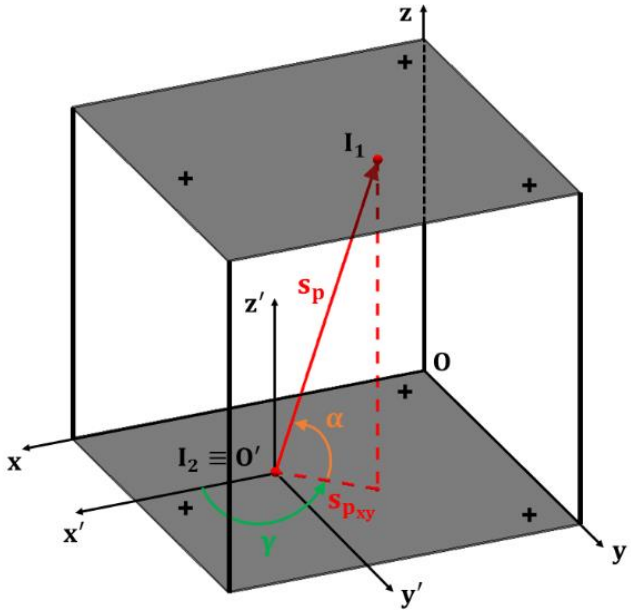

Figure 4. Coordinate systems for the estimation of the space debris direction.

The particle trajectory coincides with the direction of the vector joining points I_1 and I_2, which are the location impact on the top and bottom plates, respectively. The position vector $\mathbf{s_p}$ points from I_2 to I_1 and can be identified by the three vector components (or projections) with respect to the Oxyz axes:

$$\mathbf{s_p} = s_{p_x}\,\hat{\mathbf{i}} + s_{p_y}\,\hat{\mathbf{j}} + s_{p_z}\,\hat{\mathbf{k}}\,, \tag{10}$$

where $[\hat{\mathbf{i}} \quad \hat{\mathbf{j}} \quad \hat{\mathbf{k}}]$ represent the unit vectors of the three axes. In terms of coordinates of the two impact points, Eq. (10) can be rewritten as:

$$\mathbf{s_p} = (x_1 - x_2)\,\hat{\mathbf{i}} + (y_1 - y_2)\,\hat{\mathbf{j}} + (z_1 - z_2)\,\hat{\mathbf{k}}\,. \tag{11}$$

The magnitude (or modulus) of the position vector can be calculated as shown below:

$$s_p = \sqrt{(x_1 - x_2)^2 + (y_1 - y_2)^2 + (z_1 - z_2)^2}\,. \tag{12}$$

The unknown angles are visualised by considering a Cartesian coordinate system with the impact location at the bottom plate as the new origin, i.e. a translated system with respect to the original one. The reference direction for the azimuth angle is the *x*-axis and it is measured counter clockwise from this axis towards the *y*-axis. The three components of the position vector $\mathbf{s_p}$ are related to its magnitude by the following system of equations:

$$\begin{cases} s_{p_x} = s_p\ \cos\alpha\ \cos\gamma \\ s_{p_y} = s_p\ \cos\alpha\ \sin\gamma \\ s_{p_z} = s_p\ \sin\alpha \end{cases}. \tag{13}$$

The elevation angle α can be computed by the third equation of system (13):

$$\alpha = \sin^{-1}\left(\frac{s_{p_z}}{s_p}\right) = \sin^{-1}\left(\frac{z_2 - z_1}{\sqrt{(x_2 - x_1)^2 + (y_2 - y_1)^2 + (z_2 - z_1)^2}}\right), \tag{14}$$

whereas the azimuth angle γ can be calculated by using the first and second equation of system (13):

$$\gamma = \tan^{-1}\left(\frac{s_{p_y}}{s_{p_x}}\right). \tag{15}$$

4 ESTIMATION OF THE SPACE DEBRIS VELOCITY

Since TR method provides the impact location on both plates (see Section 3.1), it is possible to calculate the distance between the impact point and the sensor location on both plates, obtaining $N = 3$ values for r_1 and r_2. Only two elements are still unknown in the velocity formulation of the debris particle [Equation (4)]: i.e. the time difference Δt of the signals acquired by a couple of transducers located at the same positions on the two plates and the wave velocities on both plates at transducer locations. The methodology to obtain time differences Δt and wave speeds is reported in the following two sub-sections.

4.1 TIME DIFFERENCES OF ARRIVAL ESTIMATION

Several methods are present in literature to compute the time difference between measured elastic signals, which are based on direct calculation using the cross correlation technique [35] or by simple difference between TOAs. In the latter case, the objective is to estimate the TOAs with high level of accuracy [30]. The TOA, also called "onset time" of transient signals such as acoustic emissions, seismograms or ultrasound, can be described as the time when the ballistic wave originated at the impact source reaches one (or more) receiving sensor. The TOA is usually referred to as the time where the first difference between the signal and the noise takes place. The proposed research work used an estimation approach based on the Akaike Information Criterion (AIC) that, unlike traditional TOA identification techniques, it allows identifying the onset time with high accuracy in the range of microseconds. A detailed explanation of the AIC theory and derived automatic pickers able to identify the TOA of a signal is reported in [30] and [38]-[41]. The main assumption for the AIC method is to consider the signal, or a general time series, as divided in two different locally stationary segments, each modelled as an autoregressive (AR) process. The first segment is the non-informative part, and it is called "noise", while the second one is the informative part, and it is called "signal". These two datasets are separated by the onset time, which can be regarded as the global minimum of the following AIC function, called "Maeda's relation" [42]:

$$\mathrm{AIC}(k) = k \ln\big(\mathrm{var}(x[1,k])\big) + (n-k-1)\ln\big(\mathrm{var}(x[k+1,n])\big), \qquad (16)$$

where x represents the time series (the signal), k represents the range through all points of the signal and $\mathrm{var}(\cdot)$ is the sample variance of the signal. In this work the so-called "characteristic function AIC picker" based on Eq. (16) was chosen [30],[43],[44]. The name is due to a suitable mathematical function, called "characteristic function" (CF), whose purpose is to improve the resolution level between noise and signal through the enhancement of changes in signal features [45] such as the frequency, the amplitude or both. In correspondence of these changes, it is possible to detect the time of arrival of the signal. For this reason, the performance of the picker highly depends on the chosen

characteristic function. Among all characteristic functions used in literature, in this research work the following function suitable for thin plates was chosen [43],[44]:

$$\mathrm{CF(i)} = |\mathrm{x(i)}| + \mathrm{R}\,|\mathrm{x(i)} - \mathrm{x(i-1)}|\,, \tag{17}$$

where R is a constant. The algorithm is divided into two steps (see Figure 5), consisting of a first rough estimation of the onset time during the first step, with a more precise determination of it during the second step. The first step starts with the determination of a shortened time window, which is illustrated in Figure 5a as the range between the two cyan lines. The starting time was set at the beginning of the original signal within the noise level. The ending time was set after the global maximum of the characteristic function (17), $\mathrm{t_{MAX}}$, on time $\mathrm{t_{MAX}} + \Delta\mathrm{t_{AM}}$. The time delay $\Delta\mathrm{t_{AM}}$ is a value depending on the tested material, set to $20\ \mu\mathrm{s}$ for our experiment and suitable for CFRP thin-plate specimens in accordance to [43],[44]. Maeda's relation (16), with the characteristic function (17) as input, is applied to this time window so that the first onset time, $\mathrm{t_{MIN}}$, is determined. The accuracy of the AIC picker is increased by focusing on the neighbourhood of the first estimation. A new time window is considered, whose limits are $\mathrm{t_{MIN}} - \Delta\mathrm{t_{FB}}$ and $\mathrm{t_{MIN}} + \Delta\mathrm{t_{FA}}$, where the setting are $\Delta\mathrm{t_{FB}} = 30\ \mu\mathrm{s}$ and $\Delta\mathrm{t_{FA}} = 10\ \mu\mathrm{s}$, chosen according to [43], [44]. A new application of Eq. (16) on this new time window defines the actual time of arrival.

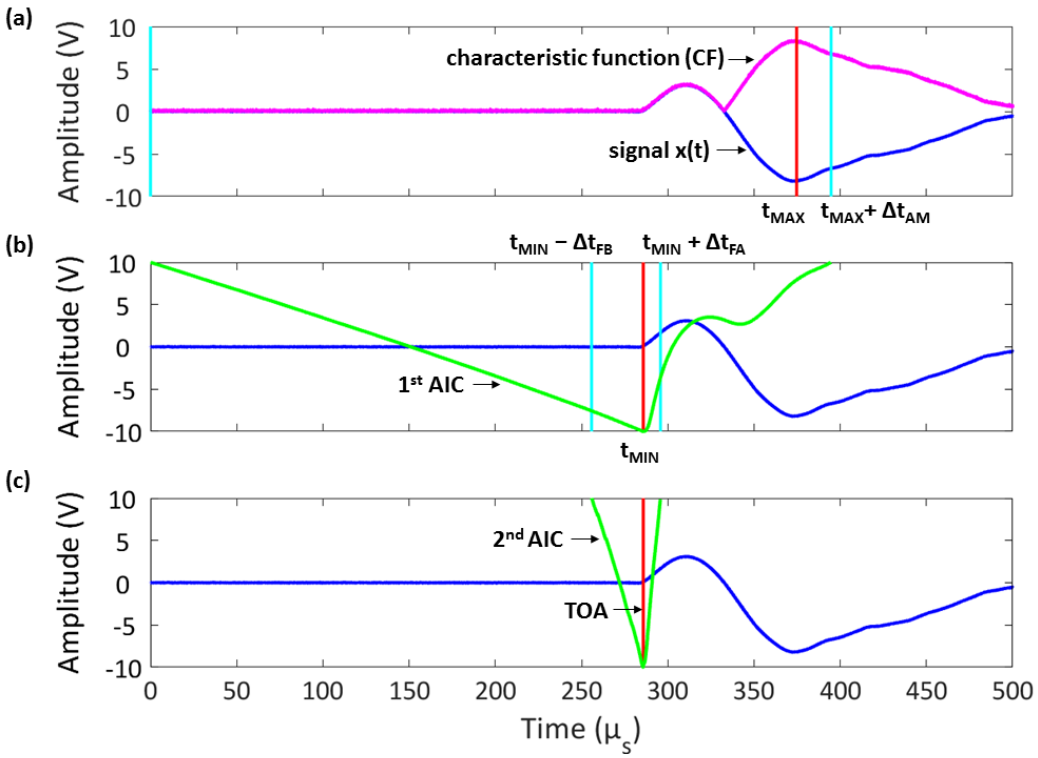

Figure 5. Visual description of CF-AIC picker: (a) determination of the initial time window; (b) estimation of the first TOA and determination of the second time window; (c) estimation of the final TOA.

4.2 WAVE VELOCITY CALCULATION

For CFRP composites with different lay-ups, the propagating wave velocity is not constant and depends on the wave propagation direction. The angular-group velocity relationship of most aeronautical cross-ply composites is defined as "elliptical" or "quasi-elliptical", i.e. the group speed versus the propagation angle θ follows an elliptical shape [46]. Group velocities or wave fronts of elliptical shape have the advantage of requiring only two velocity measurements related to the speed in the fibre direction (V_{0°) and transverse to fibres (V_{90°). The elliptical wave velocity pattern can be described by the following equation [46]:

$$V(\theta) = \frac{V_{0^\circ}\ V_{90^\circ}}{\sqrt{(V_{0^\circ}\ \sin\theta)^2 + (V_{90^\circ}\cos\theta)^2}}. \qquad (18)$$

Since the two composite plates used are identical, an initial calibration process is necessary to confirm the assumption of "elliptical angular-group velocity pattern". Following this calibration, it was possible to evaluate the velocities related to the $N = 3$ propagation angles θ, whose values are

calculated based on the fibre direction, sensor locations and the position of the acoustic source (i.e. the calculated impact). As shown in Figure 6, the angular measurements are computed counter clockwise from the longitudinal fibre direction to the line joining the acoustic source and the single receiver transducer.

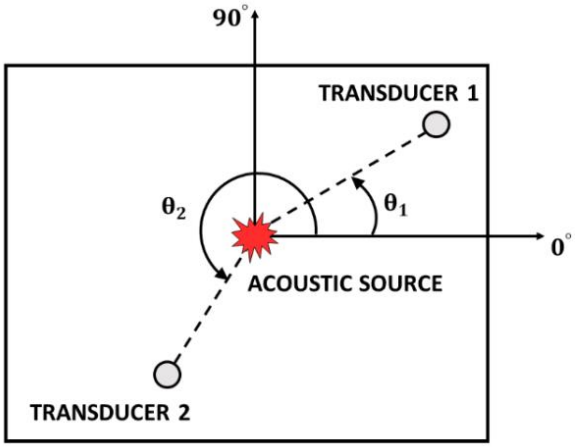

Figure 6. Reference system for the calculation of propagation angles θ.

5 EXPERIMENTAL SET-UP

Two CFRP composite plates with dimensions of $200\ \text{mm} \times 200\ \text{mm}$ were fabricated (Figure 7), each including three embedded PZT transducers for the reception of elastic waves (Figure 8a). Samples were made using four layers of unidirectional carbon/epoxy (T800/M21) prepregs. As illustrated in Figure 8b, the lay-up used was $[90^{\circ}/0^{\circ}]_s$ giving a plate thickness of around 1.3 mm. The PZTs were placed at the interface between the two middle layers during the lay-up process. To avoid the creation of short-circuits, the contact between the PZTs and the electrically conductive carbon fibres was prevented using an insulation technique proposed in a previous study of the authors [24]. Specifically, the top (conductive) surface of each PZT was covered with a single layer $(10\ \text{mm} \times 10\ \text{mm})$ of woven E-glass fibre fabric. Regarding to the wires soldered to the anode and the cathode of the PZTs, their free ends were directed outside the top surface of the plates by passing them through small incisions in the fibre directions of the two plies above the PZTs. In this way, fibre cutting was avoided and distortions of the internal plate structure were minimised. Plates were cured

using standard autoclave process for 120 minutes at a pressure of 0.7 MPa and a temperature of 150° C with a ramp rate of 3° C per minute. After completion of the curing process, the wire ends were attached to 50 Ω Bayonet Neill-Concelman (BNC) connectors using low noise cables (RG174/U).

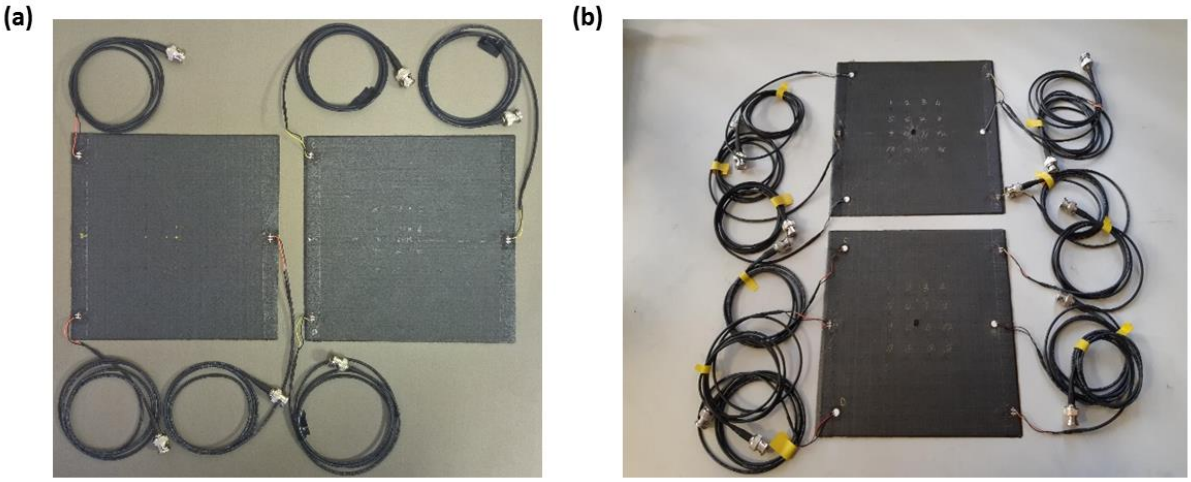

Figure 7. Manufactured CFRP composite plates with embedded PZT transducers: intact samples (a) and post-impacted samples (b).

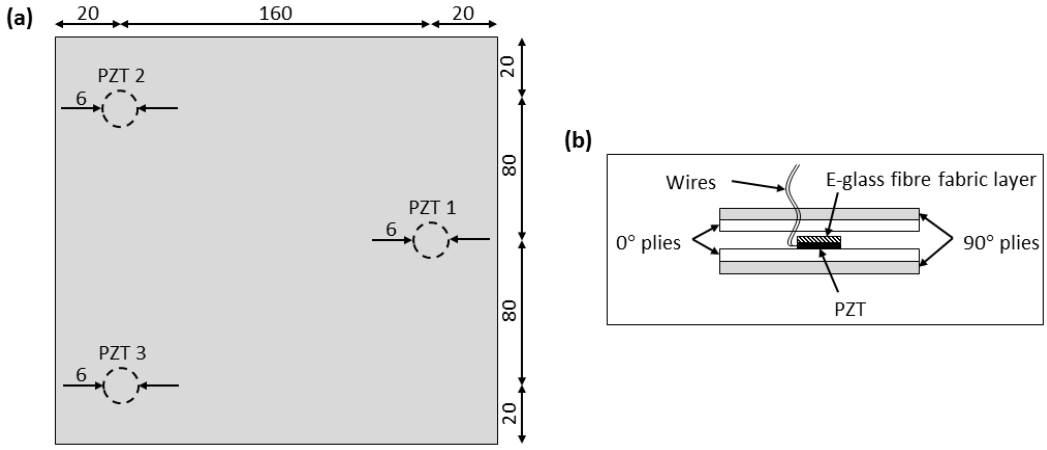

Figure 8. Positions of embedded PZTs in CFRP plate (a); lay-up of CFRP plate with embedded PZTs (b).

As reported in Section 3, for the TR process the Cartesian reference frame was chosen with the origin at the left corner of the bottom CFRP plate. The monitoring area consisted of a grid arranged with equally spaced (20 mm) nodes. As shown in Figure 11, the distance between the two parallel plates was 190 mm, and each plate was fixed at the four corners. In order to validate the experimental campaign with reproducible experiments, low-velocity impact tests were performed by using an impact machine with an impactor of around 2.7 kg instrumented with a sharp tip. The impactor was

drop from a height of 1000 mm above the top plate with a maximum impact energy of around 26 J. This allowed the impactor to reach a maximum velocity equal to 4.2 m/s (~150 km/h). As reported in Section 3.1, the use of low-velocity impacts did not compromise the validity of the proposed SCODD system. Elastic signals were acquired using two linked four-channel oscilloscope with 16 bits of resolution, a sampling rate of 2 MHz and an acquisition window of 0.2 sec. All algorithms were implemented by the authors using a MATLAB software code and the computational time is ~2 sec.

6 RESULTS

The results section is divided into two sub-sections: in Section 6.1 the material characterisation process for the wave velocity estimation is shown, whilst in Section 6.2 the results obtained from three different impact tests with different direction parameters are presented. The accuracy of the impact localisation method is expressed by the following formula for the location error, Ψ [30]:

$$\Psi = \sqrt{(x_{real} - x_{calculated})^2 + (y_{real} - y_{calculated})^2}\,, \tag{19}$$

where (x_{real}, y_{real}) are the coordinates of the true impact position and $(x_{calculated}, y_{calculated})$ are the coordinates of the impact location.

6.1 CALIBRATION ANGULAR - GROUP VELOCITY PATTERN

A calibration process necessary to evaluate the pattern of the group wave velocity in the CFRP plate was initially carried out (Figure 9). Impacts were performed at the centre of the plate by using a hand-held instrumented hammer (sensitivity factor $= 2.215 \frac{mV}{N}$) connected to a signal conditioner manufactured by Meggitt-Endevco. Two acoustic emission transducers (S_1 and S_2) of 150 kHz central frequency were placed at a distance of 50 and 70 mm from the impact location, respectively. The distance between the centres of the two transducers was around 20 mm. The direction of the wave propagation was identified by the angle between the line joining the impact point and the two transducers and the longitudinal fibre direction (0°). Four impacts were performed at each direction, starting from 0° and proceeding counter clockwise with 15° intervals, therefore 24 directions were

considered to cover all the plate. A total of 192 ($4 \times 2 \times 24$) signals were available at the end of the calibration process.

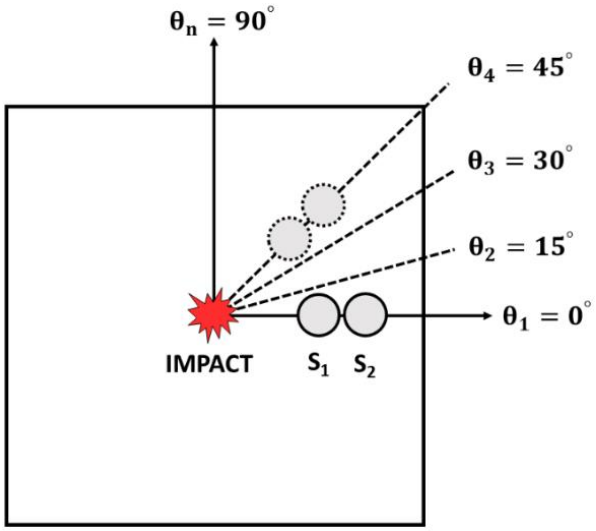

Figure 9. Experimental set-up for the material characterisation process.

Group velocities were estimated from the distance between the transducers (fixed for each direction) and the difference in TOA between the two acquired signals. TOA was calculated using the AIC picker described in Section 4.1. At each direction, the mean velocity was calculated using the four obtained values. In Figure 10, the comparison between the experimental velocity values and the theoretical ones obtained by using Eq. (18) is shown. Good agreement between the experimentally calculated values and the elliptical pattern of the wave velocity was found, with a maximum difference of ~20 m/s.

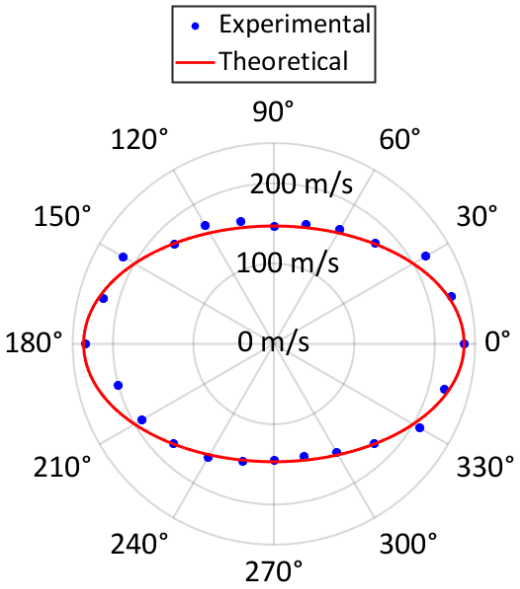

Figure 10. Comparison among the experimental wave velocity values and the theoretical ones by using Eq. (18).

6.2 SCODD TESTS RESULTS

SCODD results from three different experimental impact tests are here shown. Each test was related to the two impacts on both plates. The direction of the first impact was perpendicular to the two CFRP plates, therefore an elevation angle equal to 90° was expected, whilst the other two tests revealed elevation values associated with the geometry of both detector and impactor. It should be noted that in a space environment the high velocity of a piece of debris can be considered almost constant between the two plates, whilst in the performed experimental tests, the velocity of the impactor tip changes linearly due to the gravitational field. Hence, an average speed of the impactor was considered for the experimental tests.

6.2.1 TEST 1 – PERPENDICULAR IMPACT

Figure 11 shows the high accuracy of TR method for the impact localisation, with an error less than 1 mm for both plates [see Eq. (19) and Table 1]. A summary of results is reported in Table 1.

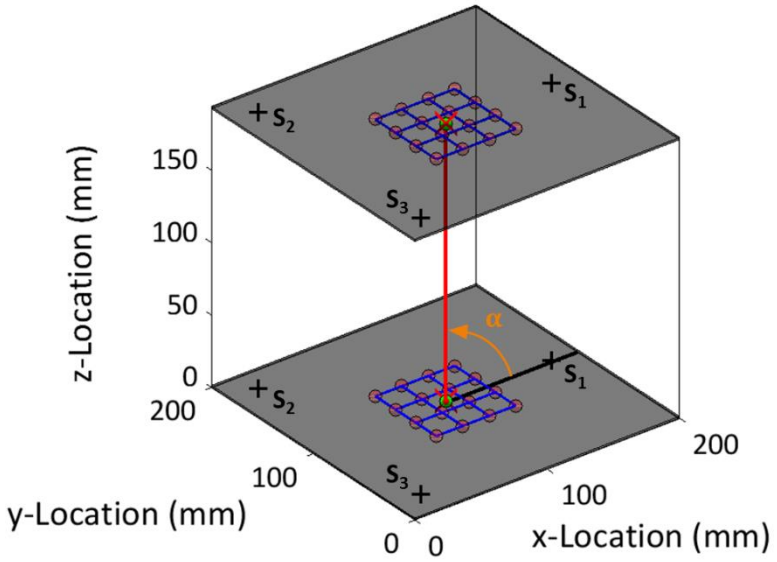

Figure 11. Test 1 – Direction and localisation of the impact on the two plates (real impact location is shown as a green circle, whilst the calculated one is depicted with a red cross). Calibration points are shown with red circles.

As expected, the elevation angle was almost 90°. Since the direction is perpendicular to both plates, each line of the reference plane (the bottom plate) passing through the impact point was used as the reference line for the calculation of the elevation angle. In Figure 11, the *x*-axis was used as reference line. As previously stated, the azimuth angle is not defined if the elevation angle is equal to 90°. The difference between the true azimuth angle (equal to 0°) and the calculated one presented in Table 1 is due to the presence of a small projection of calculated $\mathbf{s_p}$ (not perfectly perpendicular to both plates) on the reference *xy*-plane.

Table 1. Test 1 – Impact direction and localisation results.

	Top plate		Bottom plate	
	x-Coordinate (mm)	y-Coordinate (mm)	x-Coordinate (mm)	y-Coordinate (mm)
Current impact	100	100	100	100
Calculated impact	100.06	99.88	100.1	99.9
Location error Ψ (mm)	0.13		0.14	
	True		Calculated	
s_p (mm)	191.3		191.3	
Azimuth angle γ	0°		246.55°	
Elevation angle α	90°		89.96°	

The velocity values of the impacting object and the parameters necessary for their calculation are reported in Table 2. Acquired signals on both plates are depicted in Figure 12. The average value among the three calculated velocity values is around 4.35 m/s that is very similar to the mean velocity of 4.2 m/s as reported in Section 5.

Table 2. Test 1 – Impact velocities results.

	Transducer 1		Transducer 2		Transducer 3	
	Top plate	Bottom plate	Top plate	Bottom plate	Top plate	Bottom plate
d_{I-S} (mm)	79.94	79.9	113.26	113.22	113.09	113.21
θ_{I-S}	0.08°	0°	134.98°	135.03°	224.94°	224.96°
V_w (m/s)	236.36	236.36	176.25	176.33	176.36	176.33
Δt (s)	0.0439		0.0434		0.0446	
V_p (m/s)	4.36		4.41		4.29	

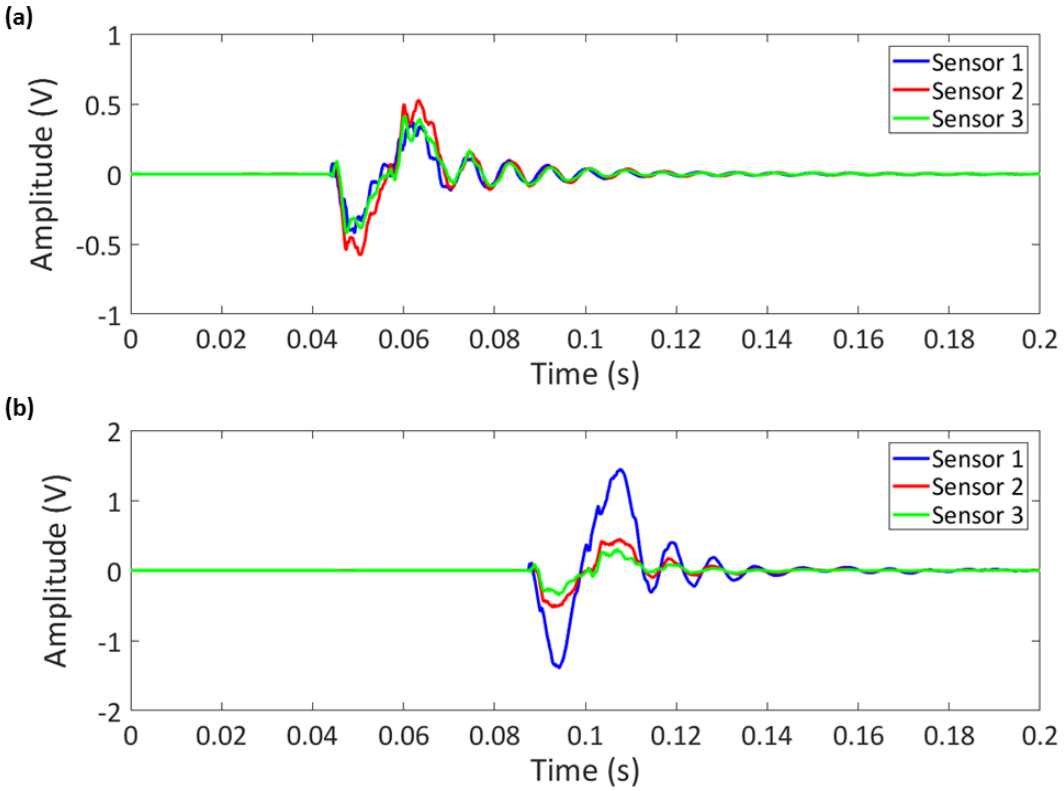

Figure 12. Test 1 – Signals acquired by transducers on the top plate (a) and on the bottom plate (b).

6.2.2 TEST 2 – SKEWED IMPACT 1

The impact test 2 is represented in Figure 13, which shows the direction of impacts, azimuth and elevation angles, the true and calculated impacts and calibration points used for the TR algorithm. Experimental results are summarised in

Table *3* and Table 4.

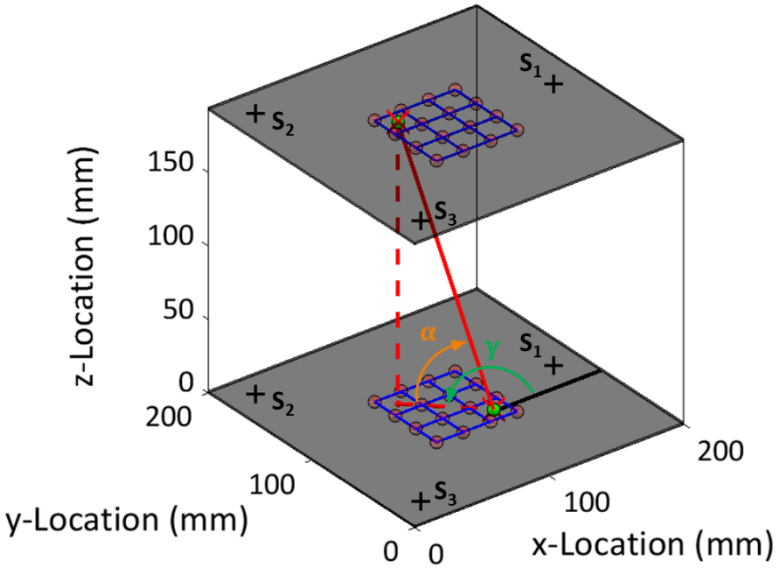

Figure 13. Test 2 – Direction and localisation of the impact on the two plates (real impact location is shown as a green circle, whilst the calculated one is depicted with a red cross). Calibration points are shown with red circles.

Table 3. Test 2 – Impact direction and localisation results.

	Top plate		Bottom plate	
	x-Coordinate (mm)	y-Coordinate (mm)	x-Coordinate (mm)	y-Coordinate (mm)
Current impact	80	120	120	80
Calculated impact	79.68	119.99	120	80.01
Location error Ψ	0.32		0.01	
	True		Calculated	
s_p (mm)	200		199.5	
Azimuth angle γ	135°		135.24°	
Elevation angle α	74°		73.47°	

Table 4. Test 2 – Impact velocities results.

	Transducer 1		Transducer 2		Transducer 3	
	Top plate	Bottom plate	Top plate	Bottom plate	Top plate	Bottom plate
d_{I-S} (mm)	102.3	63.24	84.63	141.41	116.45	116.62
θ_{I-S}	348.73°	18.42°	134.84°	135°	239.17°	210.97°
V_w (m/s)	229.47	219.52	176.06	176.28	160.21	198.17
Δt (s)	0.0472		0.0481		0.0479	
V_p (m/s)	4.21		4.18		4.15	

As in Test 1, the calculated velocities are comparable with the mean velocity between real impacts occurred on the two plates.

6.2.3 TEST 3 – SKEWED IMPACT 2

Results from the third impact test are presented in Figure 14, Table 5 and Table 6. Impactor velocities are very similar to the values obtained in the previous Test 2. This is because impacts in Tests 2 and 3 occurred in symmetrical position on both plates. Therefore elevation values are the same, whereas the azimuth angle in Test 3 is phased of 180^0 with respect to Test 2. As before, the obtained velocities are comparable to the real mean velocity between two impacts.

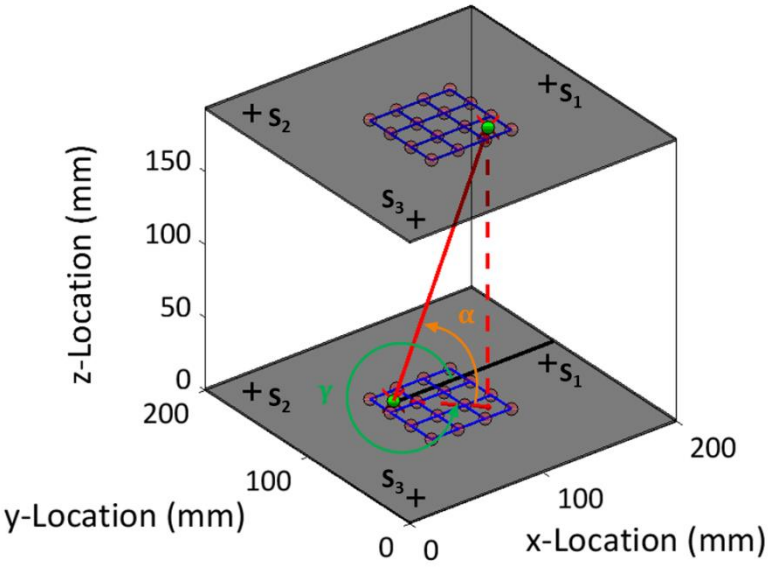

Figure 14. Test 3 – Direction and localisation of the impact on the two plates (real impact location is shown as a green circle, whilst the calculated one is depicted with a red cross). Calibration points are shown with red circles.

Table 5. Test 3 – Impact direction and localisation results.

	Top plate		Bottom plate	
	x-Coordinate (mm)	y-Coordinate (mm)	x-Coordinate (mm)	y-Coordinate (mm)
Current impact	120	80	80	120
Calculated impact	120.24	80.38	80.05	119.98
Location error Ψ	0.45		0.05	
	True		Calculated	
s_p (mm)	200		199.4	
Azimuth angle γ	315°		315.42°	
Elevation angle α	74°		73.57°	

Table 6. Test 3 – Impact velocities results.

	Transducer 1		Transducer 2		Transducer 3	
	Top plate	Bottom plate	Top plate	Bottom plate	Top plate	Bottom plate
d_{I-S} (mm)	62.9	101.92	141.32	84.9	117.02	116.63
θ_{I-S}	18.18°	348.69°	135.18°	135.02°	211.06°	239.01°
V_w (m/s)	219.9	229.43	176.52	176.3	198.01	160.36
Δt (s)	0.0471		0.0475		0.0474	
V_p (m/s)	4.25		4.17		4.21	

7 CONCLUSIONS

This paper presented the experimental results to demonstrate the proof-of-concept of a novel *in-situ* and lightweight smart composite orbital debris detector (SCODD) for the localisation of space debris impacts and the estimation of debris particles' direction and velocity. The SCODD system consisted of two fixed parallel CFPR composite plates instrumented with three embedded piezoelectric transducers. The coordinates of impact locations on both plates were calculated by processing the measured acoustic emissions with the time reversal method. The difference in arrival times between

signals acquired by two transducers at the same positions on both plates were used to compute the velocity of the particle. The Akaike Information Criterion picker was employed to determine the arrival times with high accuracy. For the estimation of the space debris velocity, a calibration process was initially performed to evaluate the angular-group velocity elliptical pattern of elastic waves propagating into the plates. A number of experimental tests with impacts applied at different directions was then performed using the SCODD system. Results indicated accurate calculation of the impact directions and velocities, thus demonstrating the effectiveness of the proposed debris detection system for future Earth satellites by reducing the risk of collision and enhancing the orbital lifetime.

ACKNOWLEDGMENTS

This paper has been funded by the EXTREME project of the European Union's Horizon 2020 research and innovation programme under grant agreement No. 636549.

REFERENCES

1. Tonetti, S., Cornara, S., Faenza, M., Verberne, O., Langener, T., & de Miguel, G. V. (2018). Active Debris Removal and Space Debris Mitigation using Hybrid Propulsion Solutions. In *Stardust Final Conference* (pp. 163-180). Springer, Cham.
2. Pelton, J. N. (2013). *Space debris and other threats from outer space*. New York: Springer.
3. Mespoulet, J., Héreil, P. L., Abdulhamid, H., Deconinck, P., & Puillet, C. (2017). Experimental study of hypervelocity impacts on space shields above 8 km/s. *Procedia Engineering*, *204*, 508-515.
4. Liu, M., Su, Z., Zhang, Q., & Long, R. (2016). Modeling hypervelocity-impact-induced shock waves for characterizing orbital debris-produced damage. *Journal of Applied Mechanics*, *83*(8), 081010.
5. Liu, M., Wang, Q., Zhang, Q., Long, R., & Su, Z. (2018). Characterizing hypervelocity (> 2.5 km/s)-impact-engendered damage in shielding structures using in-situ acoustic emission: Simulation and experiment. *International Journal of Impact Engineering*, *111*, 273-284.
6. Christiansen, E. L., Nagy, K., Lear, D. M., & Prior, T. G. (2009). Space station MMOD shielding. *Acta Astronautica*, *65*(7-8), 921-929.

7. Porfilio, M., Piergentili, F., & Graziani, F. (2004). First optical space debris detection campaign in Italy. *Advances in Space Research*, *34*(5), 921-926.
8. Lederer, S. M., Stansbery, E. G., Cowardin, H. M., Hickson, P., Pace, L. F., Abercromby, K. J., & Alliss, R. J. (2013). The NASA meter class autonomous telescope: Ascension island. *National Aeronautics and Space administration Houston TX Lyndon B Johnson Space Center*.
9. Cooke, W., Matney, M., Moorhead, A. V., & Vavrin, A. (2017). A Comparison of Damaging Meteoroid and Orbital Debris Fluxes in Earth Orbit. In *7th European Conference on Space Debris; 18-21 Apr. 2017; Darmstadt; Germany.*
10. Matney, M. J. (2017). Algorithms for the Computation of Debris Risk. In *7th European Conference on Space Debris; 18-21 Apr. 2017; Darmstadt; Germany.*
11. Krisko, P. H., Flegel, S., Matney, M. J., Jarkey, D. R., & Braun, V. (2015). ORDEM 3.0 and MASTER-2009 modeled debris population comparison. *Acta Astronautica*, *113*, 204-211.
12. Benvenuto, R., Lavagna, M., Schlotterer, M., & Theil, S. (2017). Experimental setup and tests' results for uncooperative objects capture and manoeuvring with robotic arm. In *7th European Conference on Space Debris; 18-21 Apr. 2017; Darmstadt; Germany.*
13. Astromaterials Research and Exploration Science. Hypervelocity Impact Technology: Shield Development Basic Concepts. National Aeronautics and Space Administration.
14. Palla, C., Kingston, J., & Hobbs, S. (2017). Development of commercial drag-augmentation systems for small satellites. In *7th European Conference on Space Debris; 18-21 Apr. 2017; Darmstadt; Germany.*
15. Axthelm. R., Klotz, B., Retat, I., & Schlossstein, U. (2017). Net Capture Mechanism for Debris Removal Demonstration Mission. In *7th European Conference on Space Debris; 18-21 Apr. 2017; Darmstadt; Germany.*
16. Burchell, M. J., Standen, S., Cole, M. J., Corsaro, R. D., Giovane, F., Liou, J. C., & Stansbery, E. (2011). Acoustic response of aluminium and Duroid plates to hypervelocity impacts. *International Journal of Impact Engineering*, *38*(6), 426-433.
17. Burchell, M. J., Corsaro, R., Giovane, F., Cole, M., Sadilek, A., Price, M. C., & Liou, J. C. (2013). A New Cosmic Dust Detector with a Novel Method Using a Resistive Grid Sensitive to Hypervelocity Impacts. *Procedia Engineering*, *58*, 68-76.
18. Bauer, W., Romberg, O., Wiedemann, C., Drolshagen, G., & Vörsmann, P. (2014). Development of in-situ space debris detector. *Advances in Space Research*, *54*(9), 1858-1869.
19. Forli, O. (1990). In orbit in-service inspection. *ESA, Space Applications of Advanced Structural Materials p 157-161(SEE N 91-11812 03-24).*

20. Schäfer, F., & Janovsky, R. (2007). Impact sensor network for detection of hypervelocity impacts on spacecraft. *Acta Astronautica*, *61*(10), 901-911.
21. Graziani, F., Porfilio, M., & Santoni, F. (2005) An in situ impact sensor on board a UNISAT microsatellite for monitoring the microparticles environment. *http://techrepots. larc. nasa. gov*.
22. Kobayashi, M., Krüger, H., Senshu, H., Wada, K., Okudaira, O., Sasaki, S., & Kimura, H. (2018). In situ observations of dust particles in Martian dust belts using a large-sensitive-area dust sensor. *Planetary and Space Science*, *156*, 41-46.
23. Corsaro, R. D., Giovane, F., Liou, J. C., Burchell, M. J., Cole, M. J., Williams, E. G., & Anderson, C. R. (2016). Characterization of space dust using acoustic impact detection. *The Journal of the Acoustical Society of America*, *140*(2), 1429-1438.
24. Andreades, C., Mahmoodi, P., & Ciampa, F. (2018). Characterisation of Smart CFRP Composites with Embedded PZT Transducers for Nonlinear Ultrasonic Applications. *Composite Structures*.
25. Ciampa, F., & Meo, M. (2012). Impact detection in anisotropic materials using a time reversal approach. *Structural Health Monitoring*, *11*(1), 43-49.
26. Ciampa, F., & Meo, M. (2014). Impact localization on a composite tail rotor blade using an inverse filtering approach. *Journal of Intelligent Material Systems and Structures*, *25*(15), 1950-1958.
27. Ciampa, F., Boccardi S., & Meo, M. (2016). Factors affecting the imaging of the impact location with inverse filtering and diffuse wave fields. *Journal of Intelligent Material Systems and Structures*, *27*(11), 1523-1533.
28. De Simone, M. E., Ciampa, F., & Meo, M. (2018). A hierarchical impact force reconstruction method for Aerospace composites. *AuxDefense 2018 Conference*.
29. De Simone, M. E., Ciampa, F., & Meo, M. (2018). A hierarchical method for the impact force reconstruction in composite structures. *Smart Materials and Structures*. (Accepted manuscript).
30. De Simone, M. E., Ciampa, F., Boccardi, S., & Meo, M. (2017). Impact source localisation in aerospace composite structures. *Smart Materials and Structures*, *26*(12), 125026.
31. Meo, M., Zumpano, G., Piggott, M., & Marengo, G. (2005). Impact identification on a sandwich plate from wave propagation responses. *Composite structures*, *71*(3-4), 302-306.
32. Ciampa, F., & Meo, M. (2010). Acoustic emission source localization and velocity determination of the fundamental mode A_0 using wavelet analysis and a Newton-based optimization technique. *Smart Materials and Structures*, *19*(4), 045027.
33. Ciampa, F., & Meo, M. (2010). A new algorithm for acoustic emission localization and flexural group velocity determination in anisotropic structures. *Composites Part A: Applied Science and Manufacturing*, *41*(12), 1777-

1786.

34. Ciampa, F., Meo, M., & Barbieri, E. (2012). Impact localization in composite structures of arbitrary cross section. *Structural Health Monitoring*, *11*(6), 643-655.
35. Kundu, T. (2014). Acoustic source localization. *Ultrasonics*, *54*(1), 25-38.
36. Chen, C., Li, Y., & Yuan, F. G. (2012). Impact source identification in finite isotropic plates using a time-reversal method: experimental study. *Smart Materials and Structures*, *21*(10), 105025.
37. Xu, L., Wang, Y., Cai, Y., Wu, Z., & Peng, W. (2016). Determination of impact events on a plate-like composite structure. *The Aeronautical Journal*, *120*(1228), 984-1004.
38. Akaike, H. (1973). Information theory and an extension of the maximum likelihood principle. In: BN Petrov, F Csaki, editors, *Second international symposium on information theory*, Springer-Verlag, 267-281.
39. Akaike, H. (1974). Markovian representation of stochastic processes and its application to the analysis of autoregressive moving average processes. *Annals of the Institute of Statistical Mathematics*, *26*(1), 363-387.
40. Akaike, H. (1974). A new look at the statistical model identification. *IEEE transactions on automatic control*, *19*(6), 716-723.
41. Kitagawa, G. and Akaike, H. (1978). A procedure for the modeling of non-stationary time series. *Annals of the Institute of Statistical Mathematics*, *30*(1), 351-363.
42. Maeda, N. (1985). A method for reading and checking phase times in auto-processing system of seismic wave data. *Zisin*, *38*(3), 365-379.
43. Sedlak, P., Hirose, Y., Khan, S. A., Enoki, M. and Sikula, J. (2009). New automatic localization technique of acoustic emission signals in thin metal plates. *Ultrasonics*, *49*(2), 254-262.
44. Sedlak, P., Hirose, Y. and Enoki, M. (2013). Acoustic emission localization in thin multi-layer plates using first-arrival determination. *Mechanical Systems and Signal Processing*, *36*(2), 636-649.
45. Allen, R. (1982). Automatic phase pickers: Their present use and future prospects. *Bulletin of the Seismological Society of America*, *72*(6B), S225-S242.
46. Paget, C. A., Atherton, K., & O'Brien, E. (2003, September). Triangulation algorithm for damage location in aeronautical composite structures. In *Proceedings of the 4th International Workshop on Structural Health Monitoring (F. Chang, ed.),(Stanford, CA, USA)* (pp. 363-370).